Available online at www.sciencedirect.com
SCIENCE DIRECT®
Journal of Catalysis 226 (2004) 54–68
JOURNAL OF CATALYSIS
www.elsevier.com/locate/jcat

Use of DFT to achieve a rational understanding of acid–basic properties of γ-alumina surfaces

M. Digne [a,b,1], P. Sautet [a], P. Raybaud [b,*], P. Euzen [c], H. Toulhoat [d]

[a] *Laboratoire de Chimie, UMR 5182, Ecole normale supérieure de Lyon, 46, allée d'Italie, 69364 Lyon cedex 07, France*
[b] *Direction Chimie et Physico-chimie Appliquées, Institut Français du Pétrole, 1-4, avenue de Bois-Préau, 92852 Rueil-Malmaison cedex, France*
[c] *Direction Catalyse et Séparation, Institut Français du Pétrole-Lyon, BP n° 3-69390, Vernaison, France*
[d] *Direction Scientifique, Institut Français du Pétrole, 1-4, avenue de Bois-Préau, 92852 Rueil-Malmaison cedex, France*

Received 10 February 2004; revised 16 April 2004; accepted 21 April 2004

Available online 9 June 2004

Abstract

In a recent priority communication [M. Digne et al., J. Catal. 211 (2002) 1], we proposed the first ab initio constructed models of γ-alumina surfaces. Using the same density-functional approach, we investigate in further detail the acid–basic properties of the three relevant γ-alumina (100), (110), and (111) surfaces, taking into account the temperature-dependent hydroxyl surface coverages. The simulations, compared fruitfully with many available experimental data, enable us to solve the challenging assignment of the OH-stretching frequencies, as obtained from infrared (IR) spectroscopy. The precise nature of the acid surface sites (concentrations and strengths) is also determined. The acid strengths are quantified by simulating the adsorption of relevant probe molecules such as CO and pyridine in correlation with surface electronic properties. These results seriously challenge the historical model of a defective spinel for γ-alumina and establish the basis for a more rigorous description of the acid–basic properties of γ-alumina.

Keywords: γ-Alumina; Oxide; Catalyst support; DFT calculations; Hydroxyl group; Infrared analysis; Surface acid properties

1. Introduction

γ-Alumina (Al_2O_3) is a key industrial material with numerous applications in refining and petrochemistry [1,2]. It can be used as a catalyst (for the Claus process) or, more widely, as a catalyst support. In the latter case, it enables the dispersion of various types of active phases: transition–metal sulfides, Co(Ni)MoS in hydrotreatment catalysts, and metallic alloys Pt–Re in reforming catalysts. Adding dopes can also modify the alumina surface properties: chlorine is known to enhance the surface acidity for reforming and isomerization processes, whereas sodium moderates the support acidic function. In all cases, the control of the surface site properties is fundamental; it governs the acid–basic reactions as well as the dispersion of active phases on the support.

Since the pioneering work of Lippens and de Boer [3], γ-alumina surfaces have been extensively studied by nuclear magnetic resonance (NMR) [4–7], vibrational spectroscopies [8–13], temperature-programmed desorption [14], calorimetry measurements [15–17], and electron energy loss spectroscopy (EELS) [18]. Even if these techniques improved our understanding of the γ-alumina properties, there are still some controversies, as to the interpretation of the experimental results. For instance, the nature of the surface hydroxyl groups and their relative concentrations are crucial to the understanding of acid–basic properties. Infrared (IR) spectra reveal up to seven different OH-stretching bands [19], and proton NMR experiments show two distinct peaks for pure alumina and five peaks for deuterated samples [5]. The assignment of these spectroscopic bands is generally based on qualitative criteria used to distinguish the surface species: the number of Al atoms surrounding the hydroxyl groups, the local coordination of Al atoms, the existence

* Corresponding author. Tel.: +33 (0)1-47-52-71-84; fax: +33 (0)1-47-52-70-58.
E-mail address: pascal.raybaud@ifp.fr (P. Raybaud).
[1] Current address: Direction Physique et Analyze, IFP-Lyon, BP n° 3-69390, Vernaison, France

0021-9517/$ – see front matter
doi:10.1016/j.jcat.2004.04.020

of vacancies, etc. The most popular model of assignment was given by Knözinger and Ratnasamy [10], based on an empirical estimate of the "net electric charge." This 25-year-old model is still popular, although it has been questioned by various experimental [11,19] and theoretical [20] works. The acid–basic sites have been probed mainly by the adsorption of molecules, coupled with IR analysis: a complete review of these works can be found in Ref. [19]. To investigate the acidity, carbon monoxide and pyridine are the most popular experimentally used basic probe molecules. Carbon monoxide is a weak Lewis base and preferentially adsorbs on unsaturated aluminum surface sites, leading to shifts to higher energy of the gas-phase CO-stretching frequency. Up to four distinct bands have been observed; however, there is no consensus as to the assignment and the corresponding strength of the acid site. Pyridine, a stronger base, is less sensitive to site strengths and is used to probe either Lewis or Brønsted acid sites.

Finally, the interpretation of spectroscopic data depends on the structural model chosen for γ-alumina surfaces. The empirical model of Knözinger and Ratnasamy [10], based on a defective spinel structure, gave a number of possible surface configurations without addressing their thermal stabilities and surface relaxation effects. Theoretical studies based on cluster models [21,22] suffered from the same weakness: the relative stability of the surface sites, the coverage of the sites, and their interactions were not taken into account in these approaches. Attempts using periodical models have been published: the work of Sohlberg et al. [23] overlooked the thermodynamic aspects, as well as the crucial question of surface hydroxyl groups. A recent article by Ionescu et al. [24], dedicated to the adsorption of one water molecule on octahedral defect spinel surfaces, does not account for the coverage or temperature effects.

The aim of the present work is to apply the periodic DFT methods to study the complex γ-alumina surfaces, taking into account temperature and water pressure during their preparation. Starting from a reliable model of bulk γ-alumina [25], the termination of the three most relevant (100), (110), and (111) surfaces is simulated. The question of γ-alumina nanoparticle morphology is also addressed. Adsorption of water molecules, coupled with Gibbs free energy calculations, leads to the determination of the stable hydroxyl structure and coverage as a function of temperature. Hence, we do not consider the clean oxide surface as obtained by ideally cleaving the bulk structure in vacuum, but we determine the stable chemical termination of the surface, including hydration processes, as a function of the preparation conditions. This step is fundamental for understanding the chemistry of surface species within a reacting environment. The resulting models allow the accurate assignment of the highest wavenumber region of the IR spectrum by calculating the OH-stretching frequencies. Finally, the acid–basic properties of the surface sites are studied by adsorbing probe molecules and analyzing surface electronic states. These calculated properties enable first the validation of the proposed surface models, by comparing them with experimental data, and lead to further insight into the atomic scale of chemical processes on γ-alumina surfaces.

2. Computational methods

The calculations are based on density functional theory (DFT), as implemented in the Vienna Ab Initio Simulation Package (VASP) [26,27], with the Perdew–Wang 91 (PW91) generalized gradient-corrected exchange–correlation functional [28]. The one-electron wave functions of the Kohn–Sham Hamiltonian are expanded in a plane wave basis set. Periodic boundary conditions are set, leading to an infinite periodically repeated system. The self-consistent electronic energy is obtained with an iterative matrix diagonalization scheme, based on an unconstrained band-by-band residuum minimization method. For the integration in the reciprocal space, a converged energy is reached for a k-point grid fineness of 0.05 Å^{-1}. Ultrasoft pseudopotentials are used to describe the ion–electron interactions [29]. The cutoff energy for geometry optimization is 300 eV, whereas the cutoff energy for frequency calculations is increased by 25%. For each cell configuration, atomic forces are calculated by means of the Hellmann–Feynman theorem, and the geometry optimization is performed with a conjugate–gradient algorithm.

The (hkl) surface is simulated using a slab model: slabs in the (hkl) crystallographic direction, are generated with at least eight atomic planes. A vacuum thickness of 12 Å is set between two periodically repeated slabs. Each slab is symmetrical to avoid unphysical dipole–dipole interactions between two consecutive slabs. The (de)hydration process of the oriented surfaces is described by the following equilibrium:

$$\mathrm{Surface}_{hkl} + n_{\mathrm{ads}}\mathrm{H_2O(gas)} \rightleftharpoons [\mathrm{Surface}_{hkl}, n_{\mathrm{ads}}\mathrm{H_2O}], \qquad (1)$$

where n_{ads} stands for the number of adsorbed water molecules per surface unit cell.

As explained in [20], the surface free energy, Γ_{hkl}, as a function of the hydroxyl surface coverage and temperature, is given by

$$\Gamma_{hkl} = \Gamma^0_{hkl} + \theta_{hkl}\frac{\Delta_r g_{hkl}}{2}, \qquad (2)$$

with

$$\Delta_r g_{hkl} = \Delta e_{hkl} + Ts(T) - \big[h(T) - e(0)\big], \qquad (3)$$

where s is the entropy, h the enthalpy, e the internal energy of water, and Δe_{hkl} is the mean adsorption energy at 0 K of n_{ads} water molecules on the (hkl) surface expressed per H_2O molecule. We assume that ZPE and entropy contributions are mainly due to water in the gas phase, and neglect these contributions for the condensed phases.

θ_{hkl} stands for the hydroxyl surface coverage and is equal to $2n_{\mathrm{ads}}/\mathrm{A}_{hkl}$, with A_{hkl} the geometric area of the (hkl) surface unit cell. Γ^0_{hkl} stands for the surface energy of a fully

dehydrated surface ($\theta_{hkl} = 0$), referenced to the bulk Gibbs free energy.

For a given θ_{hkl}, the lowest value of Δe_{hkl} corresponds to the stable configuration in the low-temperature limit among all the possible adsorption sites and adsorption modes of the n_{ads} water molecules. By varying θ_{hkl}, the lowest value of Γ_{hkl} corresponds to the stable hydroxylation state of the surface for a given temperature.

According to Eq. (2), we thus determine unambiguously the types and concentration of the surface species (hydroxyls, unsaturated aluminum or oxygen atoms) as a function of temperature.

The stretching frequencies of OH groups are predicted, using an harmonic approach. The Hessian matrix is calculated by a numerical finite-difference method and by displacing each ion by $+/-0.005$ Å from its equilibrium position in the three directions of space. Due to the high anharmonicity of the OH bonds, the harmonic values must be corrected by an anharmonicity term of 80 cm^{-1}, as calculated by Raybaud et al. [30] for similar OH groups of boehmite γ-AlOOH. In this former work, this approach enabled the assignment of the high-frequency region of the IR spectra corresponding to hydroxyl groups located on boehmite surfaces. It was also successfully applied for the calculation of OH frequency in zeolites [31,32]. However, it must be stressed that in the case of H bonding, the anharmonicity term can be significantly larger than 80 cm^{-1}. Hence, in what follows, no attempt will be made to calculate the frequency of any groups involved in such H bonding: for one type of such OH group, an estimate of ω is given (vide infra), while in all other cases, only hydroxyls with no H-donor character are considered.

To calculate the adsorption energies of the probe molecules, we use the following relationships:

$$\Delta_r E_{\text{ads}} = E(\text{surf} + \text{probe}) - E(\text{surf}) - E(\text{probe}), \qquad (4)$$

where $E(\text{surf})$ stands for the ab initio total energies of the surface, $E(\text{probe})$ of the isolated gas-phase molecule, and $E(\text{surf} + \text{probe})$ of the adsorbed molecule on the surface. A negative value, corresponding to an exothermic process, indicates a stable adsorption. In this case, because we are focusing on the stable adsorption configurations, whatever the coverage and temperature may be, we neglect all ZPE corrections and thermal effects.

3. Results and discussion

3.1. Why γ-alumina is not a defective spinel?

3.1.1. Bulk structural properties

The precise crystallographic structure of γ-alumina is still under debate. γ-Alumina is a metastable transition alumina obtained by calcination of a boehmite γ-AlOOH powder at 700 K. The bulk model used in Ref. [20] as well as in this study is taken from our previous theoretical investigation of the calcination of boehmite, the hydrated precursor of γ-alumina [25]. Starting from the layered structure of boehmite γ-AlOOH, the dehydration process leads to the collapse of the γ-AlOOH sheets along the b axis, together with shearing along the a axis. The resulting structure exhibits a fcc sublattice of oxygen atoms, observed on γ-alumina by XRD analysis [33]. This sublattice generates octahedral and tetrahedral interstices, to which aluminum atoms can diffuse. A wide range of aluminum atom distributions in this oxygen atom matrix was simulated in Ref. [25], and the most stable structure with 25% of tetrahedral aluminum was retained as the best model for γ-alumina (Fig. 1).

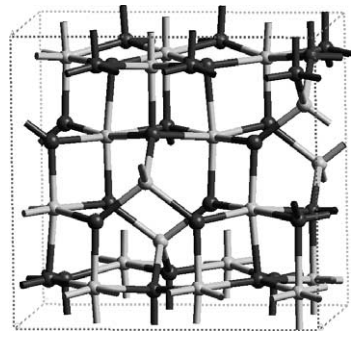

Fig. 1. Unit cell of the γ-alumina bulk according to Ref. [25]. Black balls, oxygen atoms. Gray balls, aluminum atoms.

Before our proposal [20], other theoretical as well as experimental studies relied on a defective spinel-like structure. Compared to our model, a spinel-based structure arbitrarily imposes constraints on the type and number of interstices occupied by aluminum atoms. However, in order to achieve a Rietveld refinement [33], extra-spinel sites for aluminum atoms must be assumed as in the most stable structures determined by DFT calculations [25,34]. Finally, it was found that a nonspinel model is significantly more stable than traditional spinel models (e.g., -0.05 eV/Al_2O_3 unit compared to the model determined in Ref. [35]).

Nevertheless, this model is not perfect: the typical size of γ-alumina nanoparticles is about 50 to 100 Å, and the crystallinity is poor. As a consequence, a periodic model (like ours), including 8 Al_2O_3 units, cannot entirely reproduce the complexity of this material. However, it is a good compromise between structure reliability and system sizes compatible with ab initio calculations.

Table 1 gives the complete crystallographic structure and Table 2 lists some important bulk properties compared with the experimental data. The structural parameters are close to the experimental ones: the cell volume is slightly larger (2%) within the usual GGA-DFT accuracy. Twenty five percent of the aluminum atoms are in tetrahedral sites, in agreement with NMR measurements. The simulated XRD diagram is consistent with the experimental one [25]. The model reproduces the tetrahedral distortion of the γ-alumina cell in the c direction (inherited from the c direction of the boehmite cell); this was experimentally observed, but leads to a slight expansion ($c/a = 1.02$ Å) instead of a contraction ($c/a =$

Table 1
Crystallographic structure of bulk γ-alumina, according to Ref. [25]

Space group	$P21/m$	
a (Å)	5.587	
b (Å)	8.413	
c (Å)	8.068	
β (°)	90.59	
Atom	Position	(x, y, z)
Al	2e	(0.377, 3/4, 0.126)
Al	2e	(0.868, 1/4, 0.498)
Al	2e	(0.875, 3/4, 0.125)
Al	2e	(0.615, 3/4, 0.745)
Al	4f	(0.367, 0.075, 0.612)
Al	4f	(0.116, 0.579, 0.862)
O	2e	(0.881, 3/4, 0.874)
O	2e	(0.614, 1/4, 0.640)
O	2e	(0.364, 3/4, 0.889)
O	2e	(0.132, 1/4, 0.627)
O	4f	(0.889, 0.406, 0.899)
O	4f	(0.605, 0.917, 0.614)
O	4f	(0.357, 0.406, 0.853)
O	4f	(0.138, 0.916, 0.637)

Table 2
Comparisons between bulk γ-alumina and experimental data

Properties	Calc.	Exp.
Cell volume (Å^3/Al_2O_3 unit)	47.40	46.39[a]
Al in tetrahedral site (%)	25	21-25-30[b]
Cell parameters (a, b, c) (Å)[c]	7.90, 7.93, 8.07	7.96, 7.96, 7.81[a]
Tetragonal distorsion (c/a)[c]	1.02	0.98[a]
Bulk modulus (GPa)	171	162 ± 14[d]
Electronic gap (eV)	4.9	8.7[e]

[a] Ref. [36].
[b] From NMR spectra, Refs. [37–39].
[c] a, b, c parameters refer to an ideal spinel structure (for $MgAl_2O_4$, $a = b = c = 8.08$ Å).
[d] Ref. [18].
[e] Ref. [40].

0.93–0.98 Å [36]). The calculated bulk modulus (175 GPa) matches the experimental one (162 GPa), contrary to the spinel-based models (such as defined in Ref. [35]), which lead to a larger value of 219 GPa. Furthermore, the bulk modulus is known to depend closely on the type of alumina. For instance, the calculated bulk modulus of α-alumina is about 236 GPa (exp. 254 GPa), while that of θ-alumina is 189 GPa. These numerous comparisons with experimental data underline the robustness of our bulk model, which serves as a reference for surface modeling.

3.1.2. Bulk electronic properties

The electronic density of states for bulk γ-alumina (Fig. 2) corresponds to a highly insulating oxide. The electronic gap is equal to 4.8 eV, similar to the values given by spinel-based models (4.0 [35], 4.8, 5.1 eV [41]), but far from the experimental value at about 8.7 eV [18]. However, it is well known that standard DFT methods underestimate the electronic gaps. The width of the upper valence band is about 7.8 eV and exhibits several maxima, the main one located at −1.9 eV (with respect to the Fermi level positioned at the top of the valence band). The experimental electronic structure obtained by XPS [18] exhibits an upper valence band with two maxima at −3.2 and −5.5 eV and a width of 9.5 eV, in qualitative agreement with theoretical predictions. The calculated lower valence band exhibits a main maximum at −17.6 eV, a position close to the experimental one [18] located at −20.3 eV. Our γ-alumina model gives electronic structures very similar to those of the spinel-based structures [35,41]. As a consequence, and based on this electronic analysis, the discrimination between the two models is expected to be difficult.

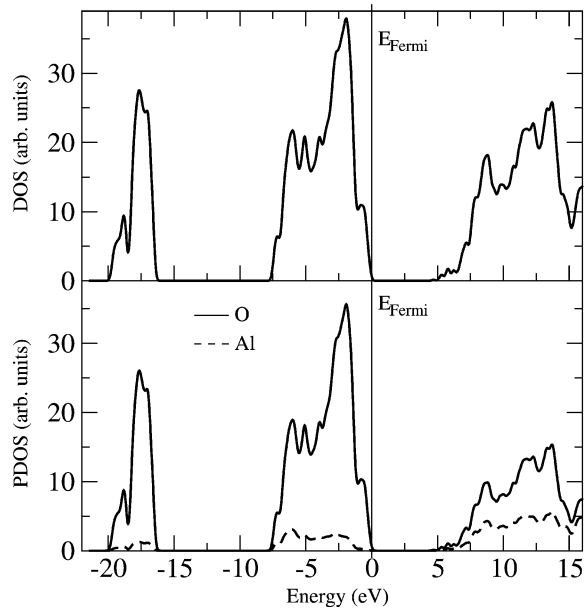

Fig. 2. Total density of states (DOS) and atom-projected density of states (PDOS) for the γ-alumina bulk model. For PDOS, the projection radii are 0.8 Å for Al atoms and 1.4 Å for O atoms.

The projected electronic density (Fig. 2) shows that the upper valence band is mainly composed of oxygen $2p$ orbitals, while the lower valence band is mainly composed of oxygen $2s$ orbitals. However, since the aluminum contributions cannot be neglected for the occupied states of the upper valence band, the O–Al bond in γ-alumina tends to be rather iono-covalent than purely ionic. Regarding the unoccupied state, the contributions of oxygen and aluminum atoms are similar.

3.2. γ-Alumina morphology

Preliminary considerations on γ-Al_2O_3 particles morphology are required, to justify the relevance of our choice for the exposed crystallographic surfaces. The morphology of γ-alumina nanoparticles depends strongly on the synthesis pathway. The standard method to recover γ-alumina is the precipitation of aluminum salts in an aqueous mother solution [2]: the formed product is boehmite (γ-AlOOH), the hydrated precursor of γ-Al_2O_3. Boehmite powders are cal-

Table 3
Structural and morphological relations between boehmite and γ-alumina

Crystallographic direction[a]			Cell parameter variation[b] (%)		Surface area (%)	
Boehmite	γ-Al_2O_3	O sublattice	Exp.[c]	Calc.	Boehmite[d]	γ-Al_2O_3[e]
(010)	(110)	Rectangular	−31	−29.3	44	53
(100)	(110)	Rectangular	−1.2	−3.6	22	21
(001)	(100)	Square	+6.0	+8.0	20	16
(101)	(111)	Hexagonal	+1.6	+3.8	14	10

[a] The crystallographic directions of bulk γ-alumina are given within the spinel orientation.
[b] Contraction (negative value) or expansion (positive value) during the transformation of boehmite into alumina.
[c] Ref. [3].
[d] Equilibrium morphology in water at 350 K according to [30].
[e] Morphology inherited from the one of boehmite [30] and using calculated values of the cell parameter variations.

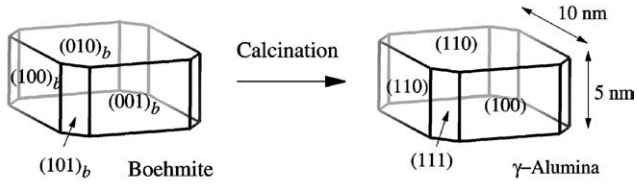

Fig. 3. Transformation of boehmite into γ-alumina nanoparticles with the corresponding surface orientations.

cinated at 700 K to produce γ-Al_2O_3. During the calcination process, the transformation is topotactic; the nanoparticle morphology remains unchanged. This important characteristic is supported by TEM observations [43] as well as X-ray diffraction data [2].

The γ-Al_2O_3 particle morphology is thus directly inherited from the equilibrium morphology of boehmite particles in an aqueous solution. The most common shape of a boehmite nanoparticle is rhombohedral: the predominant (010) surface is referred to as the basal surface, while three types of edge surfaces (100), (001), and (101) may be exposed (Fig. 3). The crystallographic analysis of the topotactic transformation shows a precise relationship between boehmite surfaces and γ-alumina surfaces. Within the crystallographic orientation using a spinel-type indexation, the topology of γ-alumina surfaces depends mainly on the fcc oxygen atom sublattice: the (100) surface exhibits a square oxygen atom sublattice, the (110) a rectangular one and the (111) an hexagonal one. According to the pseudomorphism rules, the (010) basal surface and the (100) edge surface of boehmite yield the same type of surfaces, indexed as (110) in γ-alumina. The lateral (001) and (101) surfaces of boehmite correspond to the (100) and (111) surfaces, respectively. The modifications of the lattice parameters during the transformation of boehmite into γ-alumina are well reproduced by the calculation. The main change is a strong contraction of 29% (exp. 31%) in the (010) direction, resulting from the collapse of hydrogen-bonded layers of boehmite. Taking these contraction factors together with the equilibrium morphology of boehmite particles in water, determined by ab initio simulations [30], the morphology of the formed γ-alumina particles is deduced (Table 3). The rhombohedral shape is not modified, and the relative areas of the different surfaces do not strongly change, justifying the topotactic character of the transformation. Finally, in γ-alumina, the (110) surface predominates with 74% of the total area, followed by the (100) surface (16%) and the (111) surface (10%). These theoretical predictions are in good agreement with experimental results. Using neutron diffraction analysis, Beaufils and Barbaux [42] showed that the (110) surface is estimated to be 83% of the total surface area, whereas the (100) surface is at 17%. Electron microscopy, carried out by Nortier et al. [43], confirmed that the (110) surface is the predominant facet, covering about 70% of the total surface area. The remaining 30% correspond to the (100) and (111) surfaces. One way to modify the relative areas and thus the morphology is to change either the pH or the ionic force of the aqueous mother solution during boehmite synthesis [2].

3.3. Dehydrated surfaces

Stoichiometric and fully dehydrated (*hkl*) surfaces are generated by cleaving the bulk structure along the plane defined by the (*hkl*) Miller indexes. For each surface, different ways of cutting have been tested, taking into account the different distributions of surface atoms. The structures with the lowest surface energy are considered to be the most representative of the dehydrated surface. Some of the following results obtained on the (110) and (100) surfaces have been reported in Ref. [20].

3.3.1. Local structures

(100) Surface. The stable structure of the (100) surface exhibits Al_V atoms only, i.e., fivefold coordinated aluminum (quoted as I, II, and III in Fig. 4a) and μ_3–O atoms, i.e., threefold coordinated oxygen atoms (A, B, and C). The surface density of broken Al–O bonds is low (17.1 bonds nm^{-2}), and the surface energy of the unrelaxed surface is moderate (1430 mJ m^{-2}). Surface relaxation does not drastically change the local geometry, and the surface energy decreases to 970 mJ m^{-2}.

(110) Surface. On the (110) surface (Fig. 4b), the surface density of broken Al–O bonds is higher (20.7 bonds nm^{-2}).

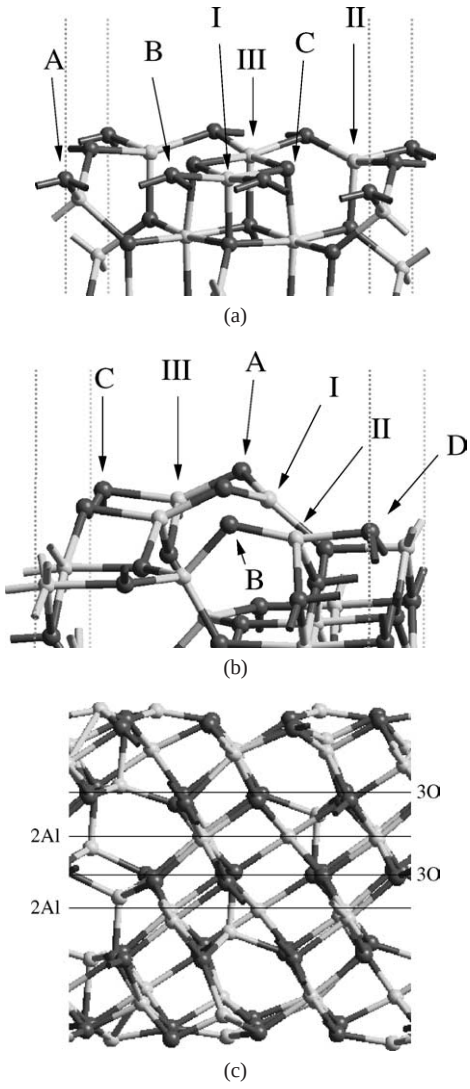

Fig. 4. Local structures of the dehydrated (a) (100) surface, (b) (110) surface, and (c) (111) surface. The relevant coordinatively unsatured surfaces sites are denoted: I, II, III for Al atoms and A, B, C, D for O atoms. Note that Al denoted II on the (100) surface is an Al_V site, even if the slightly longer fifth bond between Al(II) and O(C) is not drawn.

Compared to the (100) surface, the unrelaxed surface energy is higher (2590 $mJ\,m^{-2}$) and the surface atoms exhibit lower coordinations: Al_{IV} (II and III in Fig. 4b) for aluminum atoms inherited from bulk octahedral aluminum atoms, and Al_{III} (I) for aluminum atoms originating from bulk tetrahedral aluminum atoms, while μ_2–O (A or B), and μ_3–O (C or D) are found for surface oxygen atoms. The surface relaxation induces strong geometric modifications: the Al_{IV} atoms relax inward to reach a pseudoregular tetrahedral configuration. Besides, an upward relaxation of all oxygen surface atoms is observed. The Al_{III} (I) relaxes with its surrounding oxygen atoms (A) to form a planar AlO_3 surface species. The induced energy stabilization is large, decreasing the surface energy to 1540 $mJ\,m^{-2}$.

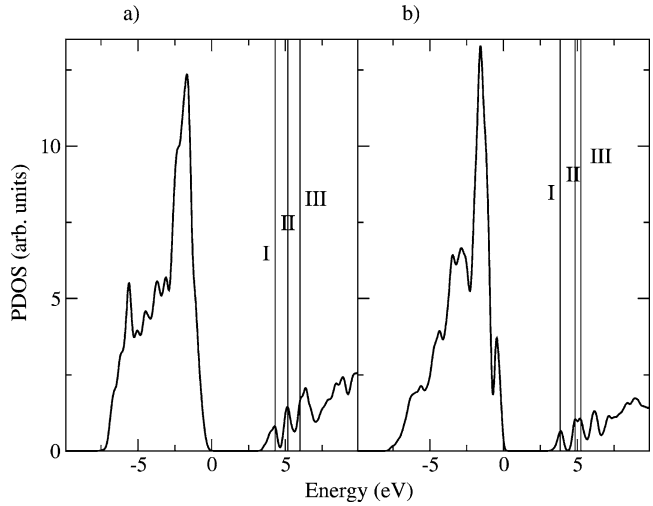

Fig. 5. Surface-projected density of states (DOS) of the (a) (100) and (b) (110) surfaces.

(111) Surface. The (111) surface is slightly different: in the (111) direction, γ-alumina exhibits alternating stacking of oxygen atoms and aluminum atoms. As a consequence, the (111) surface is polar (see Fig. 4c). This situation is very similar to the (0001) surface of α-alumina [44]. Analogous to α-alumina, we assume that the Al–O_3–$\cdots$ termination is the stable termination, avoiding the divergence of the dipolar moment within the limits of a macroscopic sample. The surface density of broken Al–O bonds is the highest (27.0 bonds nm^{-2}). As a consequence, the unrelaxed surface energy is very high (4480 $mJ\,m^{-2}$). Relaxation leads to an important decrease in the surface energy (1970 $mJ\,m^{-2}$); however, this value remains higher than that of the two other surfaces. As will be shown in Section 3.4, the fully dehydrated structure of the (111) surface cannot be stabilized under realistic conditions of temperature and partial water pressure.

3.3.2. *Intrinsic Lewis acid–basic properties and electronic surface states*

The projected electronic density of states (PDOS) on the first atomic layer of the (100) and (110) surfaces is plotted in Fig. 5. Significant differences compared to the bulk DOS appear: the surface gap is reduced to 3.5 and 3.3 eV for the (100) and (110) surfaces, respectively. Three surface electronic states, observed by EELS [18], are reported to be +2.5, +3.5, +4.8 eV above the Fermi level. The low-energy unoccupied bands (I, II, III in Fig. 5) are strongly localized in energy and space. Indeed, the energy band widths are small, estimated between 0.2 and 1.2 eV, and the charge density (Fig. 6a and 6b) is located on a single surface Al atom. Small contributions from adjacent oxygen atoms confirm the iono-covalent character of the Al–O bonds. As a consequence, a well-defined acceptor level can be attributed to each surface Al atom. Hence, bands I, II, and III in Fig. 5 correspond to Al atoms I, II, and III in Fig. 4. These discrete energy levels of the unoccupied states enable us to

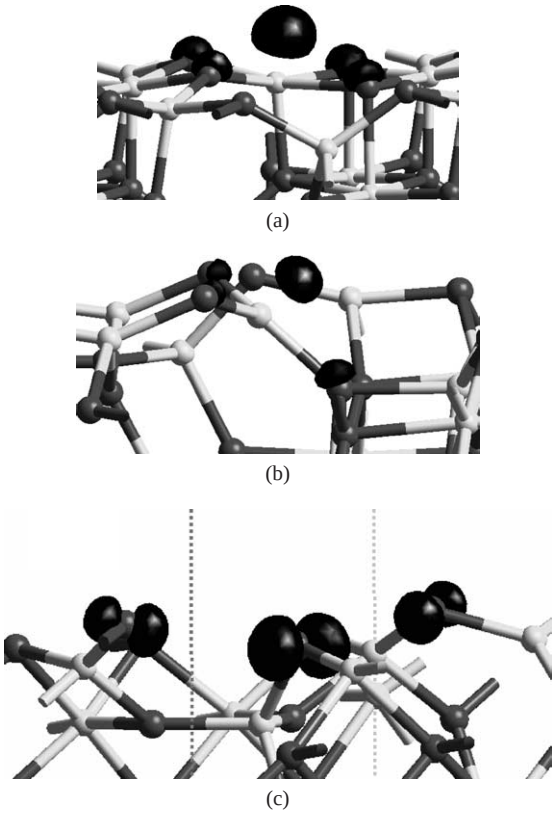

Fig. 6. Electronic density of the lowest unoccupied bands localized on the (a) aluminum (I) of the (100) surface, (b) aluminum (I) of the (110) surface. (c) Highest occupied band onoxygen (A, B, C) of the (110) surface. The density plotted corresponds to an average over all k points.

Table 4
Energetic levels of the surface aluminum Lewis sites

Surface	(110)	(100)	(110)	(110)	(100)	(100)
Site	Al_{III} (I)	Al_V (I)	Al_{IV} (II)	Al_{IV} (III)	Al_V (II)	Al_V (III)
E (eV)	−2.5	−1.6	−1.5	−1.1	−0.7	+0.1

The energy reference corresponds to the vacuum level (Roman numerals in parenthesis refer to quotes used in Fig. 4).

establish a ranking of the surface Lewis acid sites (Table 4). Such a ranking, based on a simple electronic density analysis, is defined as being intrinsic acidity, whereas the ranking obtained by probe molecule adsorption is extrinsic (see Section 3.6). As expected, the lower the Al atom coordination, the stronger, generally, the Lewis acidity. Nevertheless, some exceptions exist: the most acidic Al_V site of the (100) surface is even more acidic than the Al_{IV} site of the (110) surface. Thus, the aluminum coordination is not the only parameter relevant for Lewis acidity. Moreover, the three Al_V sites of the (100) surface exhibit energy levels ranging from −1.6 to +0.1 eV. This underlines that more subtle effects, such as the Al atom coordination sphere beyond the first neighbors or the surface electrostatic potential, may also play a role in modifying the local electronic properties.

The electronic characterization of the intrinsic Lewis basicity of oxygen surface atoms, given by the occupied electronic levels, shows that it is far more difficult to attribute one specific electronic level to each surface O atom due to the larger delocalization in energy and in space of these levels. For instance, the highest occupied band on the (110) surface (Fig. 6c) is delocalized over three distinct O atoms including μ_2–O and μ_3–O. This is also true for the (100) surface. Hence, only a global comparison between (100) and (110) surfaces is possible: the highest occupied band of the (110) surface is at −4.0 eV (with respect to the vacuum level), whereas that of the (100) surface is at −6.8 eV. In other words, the work function of the (110) surface is smaller than that of the (100) surface, meaning that the (110) surface is intrinsically more basic, in a Lewis sense, than the (100) surface. The reason can be found in the higher degree of unsaturation of the surface O atoms.

3.4. Hydration processes and thermal stability

3.4.1. (100) Surface

As explained in Ref. [20], the differential adsorption energy of water on the (100) surface as a function of the hydroxyl coverage decreases only slightly from 105 to 65 kJ mol^{-1} (see inset in Fig. 7a). Indeed, the unsaturated aluminum surface atoms are all of the Al_V type, and thus exhibit similar reactivity. The first water adsorption ($\theta_{100} = 4.3$ OH nm^{-2}) follows a dissociative mode, leading to HO–μ_1–Al_{VI} and HO–μ_2–(Al_V,Al_{VI}) groups. The water molecule is not fully dissociated, because a strong hydrogen bond remains between the two surface hydroxyl groups (d(OH···OH) = 1.64 Å). The second adsorbed molecule ($\theta_{100} = 8.8$ OH nm^{-2}) leads to the formation of three surface groups: HO–μ_3–Al_{VI}, HO–μ_1–Al_{VI}, and H_2O–μ_1–Al_{VI} (Fig. 8a). The two latter species are linked by hydrogen bonds. The next two adsorbed water molecules are not dissociated. For the fourth adsorbed molecule ($\theta_{100} = 17.1$ OH nm^{-2}) the Al–O bond is longer than in the previous cases (2.74 Å versus 1.8–1.9 Å on average) due to steric hindrance with preexisting surface OH groups. For $\theta_{100} = 17.1$ OH nm^{-2}, no more unsaturated Al surface sites are available, and the surface is covered by one water monolayer. Finally, the (100) surface is the most dense surface: about 23.4 Å^2 per Al_2O_3 unit, compared to 33.8 Å^2 per Al_2O_3 unit for the (110) surface. Thus, the stable configurations of the hydroxyls network result from the complex optimization of intrinsic acid–basic strengths of the sites, together with attractive and repulsive lateral interactions between hydroxyls.

3.4.2. (110) Surface

Compared to the (100) surface, the more adsorption energy depends strongly on the hydroxyl coverage, decreasing from 240 to 87 kJ mol^{-1} (see inset in Fig. 7b). The first adsorption mode ($\theta_{110} = 3.0$ OH nm^{-2}) is dissociative. It occurs on the Al_{III} site and on the adjacent O–μ_2–(Al_{III},Al_{IV}) site. The high exothermicity of this process (240 kJ mol^{-1}) can be explained by the strong intrinsic Lewis acidity of the highly unsaturated Al_{III} site (see Section 3.6). The fol-

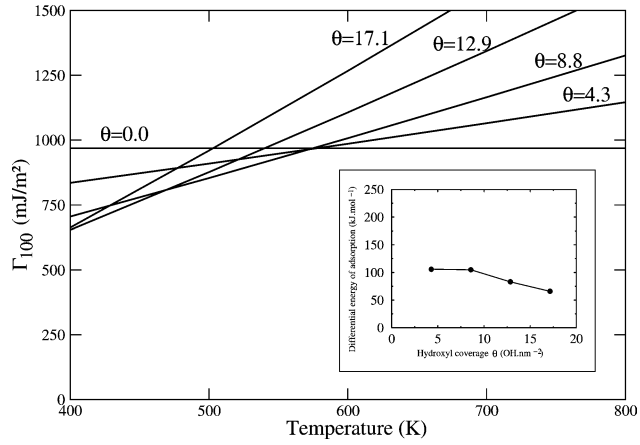

(a)

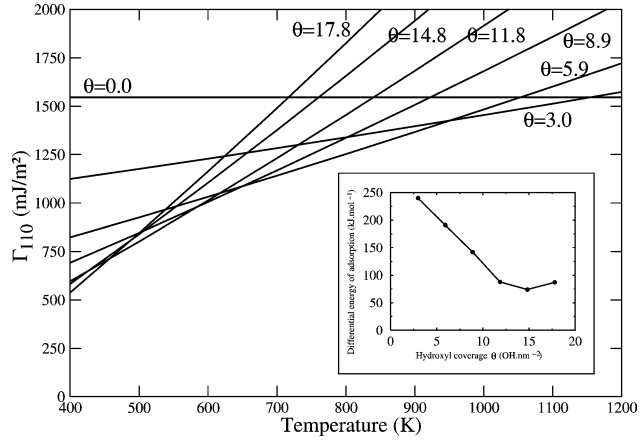

(b)

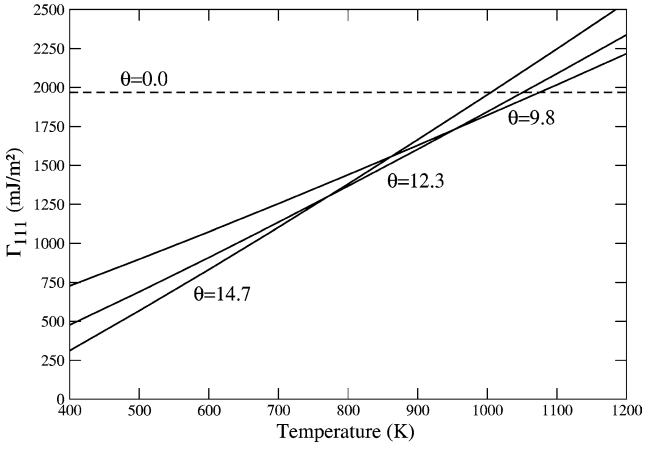

(c)

Fig. 7. Surface energy of the (a) γ-Al_2O_3(100), (b) γ-Al_2O_3(110), and (c) γ-Al_2O_3(111) surface as a function of temperature for different hydroxyl coverages (θ in OH nm^{-2}). Insets represent the absolute value of the differential energy of adsorption as a function of θ. The differential energy of adsorption is the difference between the adsorption energies of $n+1$ water molecules and n water molecules, expressed per water molecule.

lowing three water adsorptions (θ_{110} ranging from 5.9 to 11.8 OH nm^{-2}) take place on the Al_{IV} site, giving Al_V sites: HO–μ_1–Al_V, H_2O–μ_1–Al_V, and HO–μ_2–(Al_V,Al_V) on the surface (Fig. 8c). The adsorption energies are progressively reduced: 191, 141, and 88 kJ mol^{-1}. The last two adsorptions occur on these Al_V sites, forming Al_{VI} sites. The adsorption energies (74 and 87 kJ mol^{-1}) are similar to the adsorption energies on the Al_V site on the (100) surface. Finally, due to the different local environments of the Al and O surface atoms, the (110) surface exhibits a larger range of adsorption energies and a greater variety of surface hydroxyl groups.

3.4.3. (111) Surface

The approach used to study the hydration effects on the (111) surface is slightly different: it is known that a polar surface can be stabilized by adsorbing molecules present in the gas phase and, hence, modifying the surface dipole [45]. Starting from the polar stoichiometric slab Al_2–O_3–$\cdots Al_2$–O_3 (such as in Fig. 4c), water adsorption can lead to a symmetric nonpolar slab (HO)$_3$–Al_2–O_3–$\cdots Al_2$–O_3–H_3. In this case, the surface is fully hydrated. The work by Wang et al. [44] on the (0001)α-Al_2O_3 surface clearly demonstrated that the fully hydrated surface is the most stable one on a large range of water chemical potential. Using the close similarity between (0001)α-Al_2O_3 and (111)γ-Al_2O_3 surfaces, we first generated the fully hydrated state and then studied its dehydration process. The saturated surface (θ_{111} = 14.7 OH nm^{-2}) is optimized by using a simulated annealing method to find the most stable configuration (Fig. 8b). This configuration exhibits a large number of distinct surface hydroxyls, interacting through numerous hydrogen bonds (1.4 hydrogen bonds per H atom are counted, assuming that one hydrogen bond exists if d(O$\cdots$H) is smaller than 2.5 Å). The first water desorption energy is equal to 149 kJ mol^{-1} and the second one is equal to 192 kJ mol^{-1}. In this range of surface OH concentration (10–15 OH nm^{-2}), the corresponding adsorption energies for the (100) and (110) surfaces are found to be two times lower (65–88 kJ mol^{-1}). This result demonstrates the high energy cost to dehydrate the (111) surface due to the great number of hydrogen bonds and to the high coordination of the μ_2–OH or μ_3–OH groups.

3.4.4. Thermal stability

From the previously obtained adsorption energies and following the thermodynamic model described in Section 2, the surface energy is calculated for each (hkl) orientation as a function of temperature and surface OH concentrations (Fig. 7). The most stable situation corresponds to the lowest envelope of these lines, hence defining the optimal OH concentration as a function of T. The three surfaces exhibit very different thermal behaviors: the (100) surface is totally dehydrated above 600 K, whereas the (111) surface remains fully hydrated up to about 800 K; even at 1000 K the hydroxyl coverage is still high (9.8 OH nm^{-2}). The (110) surface behavior is intermediate: between 500 and 1000 K the OH concentration decreases from 11.8 to 3.0 OH nm^{-2}. The calculated surface energy is close to the experimental surface energy: from calorimetry measurements [17], the surface en-

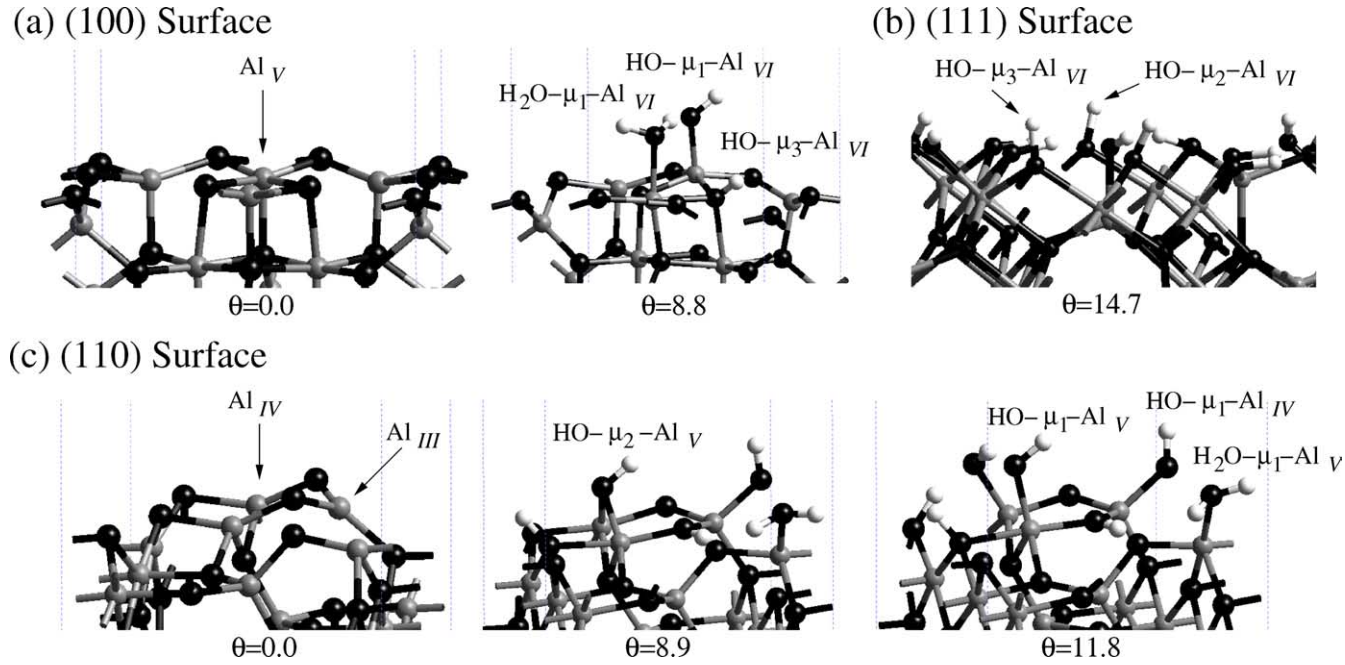

Fig. 8. Relaxed configurations of (a) γ-Al_2O_3(100), (b) γ-Al_2O_3(111), and (c) γ-Al_2O_3(110) surfaces for different hydroxyl coverages (θ in OH nm^{-2}). The most relevant surface sites are quoted: Al_n stands for aluminum atoms surrounded by n oxygen atoms, and HO–μ_m for OH groups linked to m aluminum atoms. Black balls, oxygen atoms. Gray balls, aluminum atoms. White balls, hydrogen atoms.

ergy of γ-alumina has been estimated to be 1340 mJ m^{-2} at 979 K. Assuming that this value is due mainly to the predominant (110) surface, the corresponding calculated value is 1400 mJ m^{-2}. Hence, an ab initio calculation is an accurate and efficient approach for determining surface energies, which remains a very difficult task under experimental conditions. Low temperatures (or high water partial pressure) favor the (110) and (111) surfaces, which are stabilized by the surface hydroxyl condensation. In contrast, high temperatures (or low water pressure) favor the poorly hydroxylated (100) surface. At intermediate temperatures (600 to 700 K), corresponding to standard hydrotreatment temperatures, the three surface energies are close to 1000 mJ m^{-2}.

We observe that the relative ranking of surface energies depends on the temperature. The morphology of γ-alumina nanoparticles, inherited from boehmite nanoparticles, exhibits 74% of the (110) surface, 16% of the (100), and 10% of the (111) surfaces (Table 2). According to the calculated surfaces energies for the temperature range used during the γ-alumina synthesis, the observed morphologies are thus metastable. This implies clearly that the shape of the nanoparticles is mainly fixed at the boehmite precursor stage. As a consequence, the shape of the final γ-alumina particles can be modified by changing the experimental conditions (T, pH, ionic forces, etc.) imposed in the mother aqueous solution where boehmite is synthesized [2]. Another experimental method for changing the morphology is to choose a different synthesis pathway. In the thermal oxidation of aluminum foils, the particles exhibit a totally different morphology [18]: 80% (100) surface, 10% (110) surface, and 10% (112) surface. This morphology is closer to the thermodynamic equilibrium morphology in vacuum, where the dehydrated (100) surface exhibits a lower surface energy than the dehydrated (110) surface (as shown in Section 3.3).

3.4.5. Conclusion

The hydration processes are thus crucial to the analysis of the surface properties on γ-alumina. The nature and the concentration of exposed surface sites are highly dependent on the working conditions. Temperature modifies the number of free Lewis surface sites (i.e., unsaturated Al atoms) and their nature (Al_{III}, Al_{IV}, Al_V). At the same time, the Brønsted acidity depends on the concentration and the nature of stable hydroxyl groups at a given temperature. To further validate our model surfaces and characterize the acid–basic properties, we have calculated hydroxyl-stretching frequencies (Section 3.5) and probe molecule adsorptions (Section 3.6).

3.5. Vibrational analysis of OH-stretching frequencies

Vibrational analysis is performed for the stable surfaces at 500 K, which is a standard pretreatment temperature of γ-alumina, prior to IR spectroscopic measurement. The vibrational frequencies of the surface hydroxyl groups are reported in Table 5 for frequencies higher than 3550 cm^{-1}. Indeed, a great number of hydroxyl groups are hydrogen bond donors. A strong downward frequency shift is thus observed: on the (110) surface, the free HO–Al_{IV} exhibits a frequency at 3842 cm^{-1}, whereas the frequency of a similar group, involved in a hydrogen bond, is shifted down to about 3200 cm^{-1}. Hence, hydrogen bonds have a signifi-

Table 5
Vibrational stretching frequencies of surface hydroxyl groups obtained for $\theta_{110} = 11.8$, $\theta_{100} = 8.8$, and $\theta_{111} = 14.7$ OH nm^{-2}

Site	Surface	d(OH) (Å)	ω_{cal} (cm^{-1})	$\omega_{exp.}$ (cm^{-1})	Knözinger's assignment
HO–μ_1–Al$_{IV}$	(110)	0.984	3842	3800–3785	HO–μ_1–Al$_{VI}$
HO–μ_1–Al$_{VI}$	(100)	0.988	3777	3780–3760	HO–μ_1–Al$_{IV}$
HO–μ_3–Al$_{VI}$	(111)	0.988	3752	3745–3740	HO–μ_2–(Al$_{VI}$,Al$_{VI}$)
HO–μ_1–Al$_V$	(110)	0.988	3736	3735–3730	HO–μ_2–(Al$_{VI}$,Al$_{IV}$)
HO–μ_2–Al$_V$	(111)	0.990	3732		
H$_2$O–μ_1–Al$_V$	(110)	0.988/1.093	3717		
HO–μ_1–Al$_{VI}$	(111)	0.992	3713		
HO–μ_2–Al$_{VI}$[a]	(110)	0.991	3707	3710–3690	HO–μ_3
HO–μ_2–Al$_{VI}$	(111)	0.993	3690		
HO–μ_2–Al$_{VI}$	(111)	0.993	3641		
H$_2$O–μ_1–Al$_{VI}$	(100)	0.992/1.096	3616		
HO–μ_3–Al$_{VI}$	(100)	0.997	3589	3650–3590	H bonded

[a] OH group stable for a low hydroxyl coverage ($\theta_{110} = 8.9$ OH nm^{-2}).

cant influence on the OH frequencies. The large number of OH groups involved in different hydrogen bonds explains the broad feature in the experimental spectra in the range 3000–3500 cm^{-1} in the case of highly hydrated surfaces. According to the remark made in Section 2, in what follows we focus on the OH groups which are not hydrogen bond donors and are clearly located in the high-frequency region of the IR spectra (i.e., above 3500 cm^{-1}). For these groups, it can be first easily verified that a quasilinear relationship is observed between the equilibrium O–H distances (also reported in Table 5) and the calculated stretching frequencies.

Taking into account the morphology of γ-alumina, the surface concentrations of the OH groups located on the (110), (100), and (111) surfaces are 1.1, 0.3, and 0.1 OH nm^{-2}, respectively. As a consequence, the IR bands assigned to groups located on the (100) and (110) surfaces should have a higher contribution than those on the (111) surface. The OH-stretching frequencies of the (110) and (100) surfaces have been given in detail in Ref. [20]: among the four highest frequencies, three are assigned to HO–μ_1 groups. The HO–μ_1–Al$_{IV}$ group exhibits the highest frequency (3842 cm^{-1}) followed by the HO–μ_1–Al$_{VI}$ group of the (100) surface (3777 cm^{-1}), and the HO–μ_1–Al$_V$ group on the (110) surface (3736 cm^{-1}). The multicoordinated OH groups exhibit lower frequencies: 3707 cm^{-1} for the HO–μ_2–Al$_V$ on the (110) surface and 3589 cm^{-1} for the HO–μ_3–Al$_{VI}$ of the (100) surface. These five OH groups are unambiguously assigned to the five IR bands, widely reported in the literature (Table 5). However, up to 10 distinct experimental bands have been reported [8]: their number and intensity depend on the given γ-alumina samples. In particular, a band at 3745–3750 cm^{-1} is often present in IR spectra. From our calculation, the closest frequency is obtained at 3752 cm^{-1} for the HO–μ_3 group of the (111) surface. Although this assignment might seem surprising within the Knözinger view, it is fully consistent with recent DFT work by Wang et al. [44], who found similar types of hydroxyls on (0001)α-Al$_2$O$_3$. Experimentally, a band at 3742 cm^{-1} is found on (0001)α-Al$_2$O$_3$ as reported in [19]. As a consequence, we suggest that the band at 3745–3750 cm^{-1} must be a signature of the (111) surface. Furthermore, on the (111) surface, the frequency ranking is not as expected: the highest frequency corresponds to the HO$-\mu_3$ group, followed by HO–μ_2 and HO–μ_1. In fact, for these groups, the key factor determining the frequency is not the OH coordination, but the existence of hydrogen bonds. For instance, the HO–μ_3 group is the only one not involved in a hydrogen bond (acceptor or donor), thus explaining its high frequency. Moreover, the frequencies of hydroxyls belonging to the (111) surface overlap with those of the (100) and (110) surfaces. Thus, it may be difficult to clearly identify the band assigned to the (111) surface.

Finally, the theoretical assignment proposed for the first time in [20] is confirmed and implies a significant revision of the Knözinger model [10]. To some extent, it appears closer to the assignment made by Busca et al. [11], without requiring the presence of vacancies or defects. This detailed spectroscopic analysis strongly supports the validity of our γ-Al$_2$O$_3$ model, not based on a defective spinel structure but rather on the structure established in [25]. Furthermore, we show how IR spectra may be sensitive to the nature and the relative area of exposed surfaces.

3.6. Adsorption of basic probe molecules

In order to further characterize the surface acid properties, we simulated the adsorption of two basic probe molecules (carbon monoxide and pyridine) on different γ-alumina acid sites. Carbon monoxide is a weak Lewis basis and is widely used to probe Lewis acidity on oxide surfaces. Pyridine exhibits a stronger basicity than carbon monoxide: it is more sensitive to weak acid sites such as hydroxyl groups. As shown in the previous section, the surface hydroxyl coverage and, hence, the acidic properties are highly dependent on temperature. As a consequence, surfaces with various hydroxyl coverages are probed in order to evaluate all the possible surface acid sites. The adsorption energies of the probe molecules (CO or pyridine) are calculated in order to obtain the extrinsic acid strength of the different surface sites. A detailed frequency analysis of the relevant

adsorption configurations is compared with the available experimental data.

3.6.1. CO adsorption

Carbon monoxide adsorption has been widely used to characterize the Lewis acidity of transition aluminas [46–49]. The CO-stretching frequencies are highly sensitive to the chemical environment. The σ-donation from the 5σ CO-orbital to the empty $3p$ orbitals of the unsaturated Al atoms is the driving force for the adsorption. The 5σ CO-orbital is slightly antibonding: upon surface adsorption this orbital becomes depopulated, and the CO bond is stronger as revealed by an increase in the gas-phase CO-stretching frequency. The more acidic the Al site, the higher the upward shift of the CO frequency. Four distinct bands are usually observed: (A) 2240–2220, (B) 2200–2190, (C) 2165–2155, and (D) 2150–2140 cm^{-1}. Band (D), hardly shifted with respect to CO gas, is commonly assigned to physisorbed molecules [46] or hydrogen-bonded molecules [49]. There is no consensus as to the assignment of the other three bands. According to Zecchina et al. [46], the highest band (A) is assigned to adsorption on acid surface defects, the second one (B) to tetrahedral Al atoms, and the third one (C) to octahedral Al atoms.

To simulate CO adsorption, an extended plane wave basis set is required to obtain a reliable description of the CO double bond. With an energy cutoff of 400 eV, the equilibrium CO distance is 1.145 Å and the CO-stretching frequency, calculated within a Morse approach, is 2106 cm^{-1}, which leads to an error smaller than 2% compared to the experimental values: $d(CO) = 1.128$ Å, $\omega(CO) = 2143$ cm^{-1}. The following reference temperatures are used to describe the range of possible surface sites: at 500 K corresponding to $\theta_{100} = 8.8$ and $\theta_{110} = 11.8$ OH nm^{-2}, and at 800 K corresponding to $\theta_{100} = 0.0$ and $\theta_{110} = 4.3$ OH nm^{-2}. We also consider the fully dehydrated (110) surface ($\theta_{110} = 0.0$ OH nm^{-2}) to be stable at very high temperatures (above 1100 K).

First, the CO molecule is adsorbed on unsaturated Al atoms sites. The results are given in Table 6 where the stretching frequency shift of the adsorbed CO is given with respect to the gas-phase state. The expected trend is verified: the higher the degree of unsaturation for the aluminum atoms, the more exothermic the adsorption, and the larger the upward frequency shift. According to Table 6, we assign the observed CO frequency shifts. The calculated adsorption energies are also compatible with those obtained by calorimetry measurements and reported in [46,49]. Nevertheless, the correlation between adsorption energy and frequency is not linear. Linearity is obtained only for a given surface (Fig. 9). For the fully dehydrated surfaces, the adsorption energy ranking correlates perfectly with the intrinsic Lewis acidity measured by the energy difference of the frontier orbitals (Fig. 10). For instance, the Al_V site of the (100) surface and Al_{IV} on the (110) surface exhibit similar energetic levels (−1.6 and −1.5 eV, respectively), and lead to close adsorption energies (−43 and −40 kJ mol^{-1}, respectively). Furthermore, the effect of hydration is clearly shown in Fig. 9. For the (100) and (110) surfaces, the hydration decreases not only the number of free Lewis acid sites but also the strength of the remaining Lewis acid site. This means that hydration modifies quantitatively and qualitatively the surface Lewis acidity. If we consider the CO frequency shift as a measure of the extrinsic Lewis acidity, the (110) surface appears to be more acidic than the (100) surface. This is consistent with the electronic analysis of the unoccupied states (Section 3.3.2). The effect of

Table 6
CO adsorption on Lewis and Brønsted acid sites for different hydroxyl coverages

Site	Surface	θ (OH nm^{-2})	$\Delta_r E$ (kJ mol^{-1})	$\Delta\omega$(CO) (cm^{-1})
Al_{III}	(110)	0	−76	+65
Al_{IV}	(110)	0	−43	+45
Al_{IV}	(110)	0	−26	+34
Al_V	(100)	0	−40	+15
Al_V	(100)	0	−22	+16
Al_V	(100)	0	−20	+10
Al_V	(100)	8.8	−15	−7
Al_V	(100)	8.8	−4	−11
Al_V	(110)	5.9	−29	+48
Al_{IV}	(110)	5.9	−10	+29
Al_{IV}	(110)	5.9	−10	+24
Al_V	(110)	11.8	−12	+10
Al_V	(111)	12.3	−18	−82
HO–μ_3	(100)	8.8	−11	−12
HO–μ_1	(100)	8.8	−13	+16
HO–μ_1	(110)	11.8	−6	+3
HO–μ_3	(110)	11.8	Desorption	0

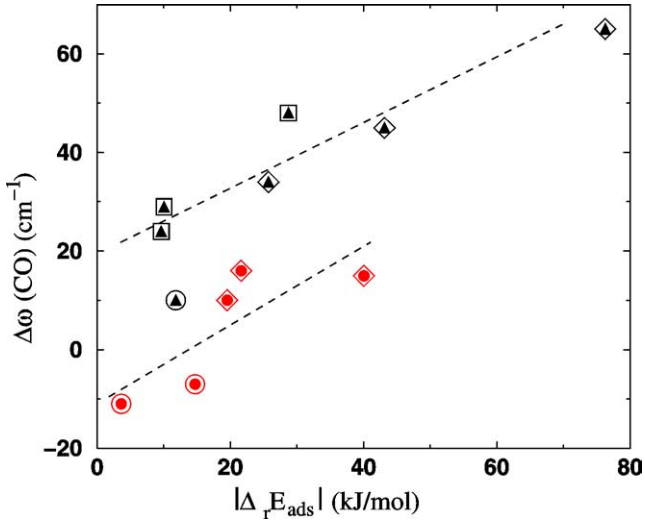

Fig. 9. Correlation between the CO adsorption energy (in absolute value) and the stretching frequency for the (100) surface (full circles) and (110) surface (full triangles). For the two surfaces, the lowest hydration state is represented by diamonds, the highest hydration by empty circles, and intermediate hydration by empty squares.

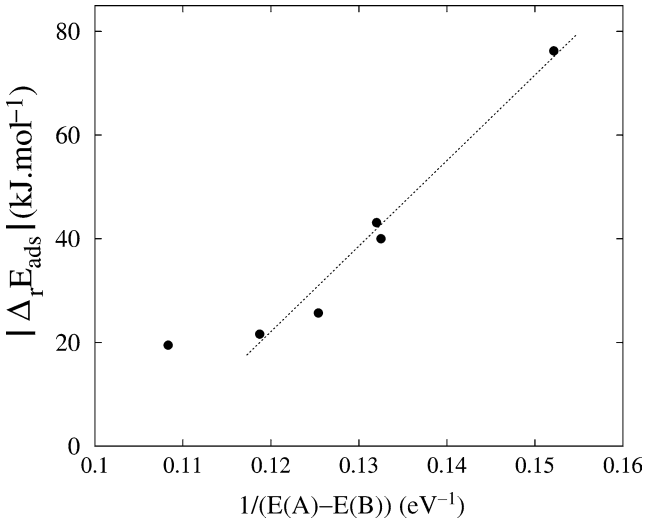

Fig. 10. Correlation between the CO adsorption energy and the frontier orbital energy difference (occupied 5σ for CO and vacant "$3p$" acceptor level of the chosen surface aluminum atom).

hydration is globally to decrease the CO frequency shift and thus the Lewis acidity. The case of the (111) surface is again more specific. Within usual temperatures, no Lewis site is present on this surface. One single Al_V Lewis acid site can be formed at high temperatures for $\theta_{111} = 12.3$ OH nm^{-2}. A low adsorption energy and a surprising strong downward shift of the CO frequency (-82 cm^{-1}) are calculated in this case. According to the high concentration of OH groups, the absorbed CO molecule is very close to one neighboring hydroxyl group (2.33 Å). Hence, a lateral interaction is added to the σ-donation: the backdonation originates from the lone pair of the surface O atoms into the empty 2π orbitals of CO. This backdonation effect is responsible for the downward shift of the frequency. Such a frequency shift has never been observed on aluminas so far, implying that usually the (111) surface is usually fully hydrated. As a consequence, the (111) surface exhibits the weakest Lewis acidity in terms of the number of sites and the strength of the site measured by the CO shift. To a lesser extent, this phenomenon also takes place for the (100) Al_V sites, which exhibits a downward shift (-11 and -7 cm^{-1}) at $\theta_{100} = 8.8$ OH nm^{-1}. It can be considered to be a signature of highly hydrated surfaces, where lateral interactions occur between adsorbed CO and surface OH groups.

The CO adsorption was also performed on some surface hydroxyl groups: the adsorption energies are low, and spontaneous desorption occurs in one case. The CO frequency is close to that of isolated CO molecule. No significant charge transfer is found: the adsorption is mainly due to electrostatic interactions [49]. For the HO–μ_3 on the (100) surface, a downward shift is observed; this is again induced by the backdonation effect of the neighboring O atoms. This downward shift is enhanced on the HO–μ_3 because of their buried location on the hydroxylated surfaces which implies a screening effect by the other neighboring hydroxyls (see also next paragraph).

Finally, a proposed assignment for the experimental IR bands on γ-alumina is given in Table 7. According to our calculations, the two highest frequencies (bands A and B) correspond to the Al_{III} sites and Al_{IV} sites, respectively, both located on the (110) surface, while the third frequency (band C) corresponds to Al_V sites of the dehydrated (100) surface. The last band D can be assigned to different weak acid sites as Al_V sites or hydroxyl groups of the (110) and (100) hydrated surfaces. The average adsorption energy of each band is also in agreement with calorimetry measurements [46,49].

Again, the consistency of the simulations of the hydration processes and CO adsorption must be stressed. According to the thermal stability, Al_{III} sites are only available above 1100 K. The corresponding CO band at 2230 cm^{-1} is observed only on γ-alumina submitted to a high-temperature pretreatment. A further interesting application of this work concerns the γ-alumina to δ-alumina transformation. IR spectroscopy shows two important modifications between the two polymorphs: the hydroxyl band at 3770 cm^{-1} [50] and the absorbed CO band at 2160 cm^{-1} disappear on δ-alumina samples [47]. According to our previous analysis, both IR bands correspond to surface species located on the (100) surface (HO–μ_1–Al_{VI}, and Al_V–CO). This implies that the (100) surface is not exposed on δ-alumina nanoparticles. This is consistent with experimental data [2], which interprets the γ to δ transition as resulting from sintering of γ-alumina nanoparticles along the (100) surfaces.

3.6.2. *Pyridine adsorption*

Pyridine is more basic and more sensitive to weak acid sites. Pyridine adsorption modes are well characterized by IR spectroscopy: in the region of 1400 to 1650 cm^{-1}, four bands $8a$, $8b$, $19a$, and $19b$, corresponding to ring vibrational modes, may be perturbed according to the nature and the acid site strength. According to the literature [19], the $8a$ band is the most sensitive.

Adsorption energies and vibrational frequencies of pyridine are calculated for different surface sites (Table 8). For a given surface, the stronger adsorption energy is obtained for the unsaturated Al_{IV} atoms. However, contrary to CO adsorption, the orders of magnitude are similar, due to the stronger basicity of pyridine. For instance, on the (100) surface and for $\theta_{100} = 8.8$ OH nm^{-2}, the Al_V acid Lewis site has an adsorption energy of -38 kJ mol^{-1}, whereas on the HO–μ_1 Brønsted site the adsorption energy is -32 kJ mol^{-1}. As a consequence, by increasing the pyridine pressure, adsorption may occur on both Lewis and Brønsted acid sites.

Concerning the vibrational properties, the calculated frequencies of the gas-phase pyridine molecule are in good agreement with experimental values. When pyridine is adsorbed on alumina surfaces, our calculations confirm that the frequency of the $8a$ band is the most sensitive to the nature of the acid site. Even if the $19a$ band is also slightly shifted (as observed experimentally), the frequency shifts of the $8b$,

Table 7
Assignment of CO adsorbed stenching frequencies and adsorption energies

Band[a]	$\Delta\omega_{exp}$[a] (cm^{-1})	$\Delta\omega_{calc}$ (cm^{-1})	$\Delta_r E_{exp}$[a] ($kJ\,mol^{-1}$)	$\Delta_r E_{calc}$ ($kJ\,mol^{-1}$)	Assignment (present work)
A	[90; 57]	65	[−85; −50]	−76	Al_{III}(110)
B	[67; 41]	[48; 24]	[−65; −35]	[−43; −10]	Al_{IV}(110) and Al_V(110)
C	[22; 11]	[16; 10]	[−45; −20]	[−40; −20]	Al_V(100)
D	[0; −8]	[10; −12]	–	[−11; −3]	Al_V (on highly hydrated surf.) or Brønsted sites

[a] Average values taken from the literature, such as in [46,49].

Table 8
Frequencies of adsorbed pyridine for different adsorption sites of the (100) and (110) surfaces for $\theta_{100} = 8.8$ and $\theta_{110} = 3.0$ OH nm^{-2}

Adsorption site	d(N···Al)	d(N···H)	d(OH)	$\Delta_r E$	ω_{8a}	ω_{8b}	ω_{19a}	ω_{19b}	ω(OH)
	(Å)			($kJ\,mol^{-1}$)	(cm^{-1})				
Isolated Pyr (Exp.[a])					1574 (1581)	1579 (1574)	1435 (1482)	1418 (1437)	
Pyr···Al_{IV} (110)	2.056	–	–	−55	1617	1586	1465	1436	–
Pyr···HO–μ_1–Al_{IV} (110)	–	1.626	1.019	−40	1610	1591	1453	1429	3201
Pyr···Al_V (100)	2.142	–	–	−38	1606	1579	1448	1424	–
Pyr···HO–μ_1–Al_{VI} (100)	–	1.770	1.019	−32	1593	1586	1450	1423	3083
Pyr···HO–μ_3–Al_{VI} (100)	–	2.742	0.998	−10	1591	1586	1452	1423	3580

[a] According to D.R. Lide, Handbook of Chemistry and Physics, 76th ed., CRC Press, New York, 1995–1996.

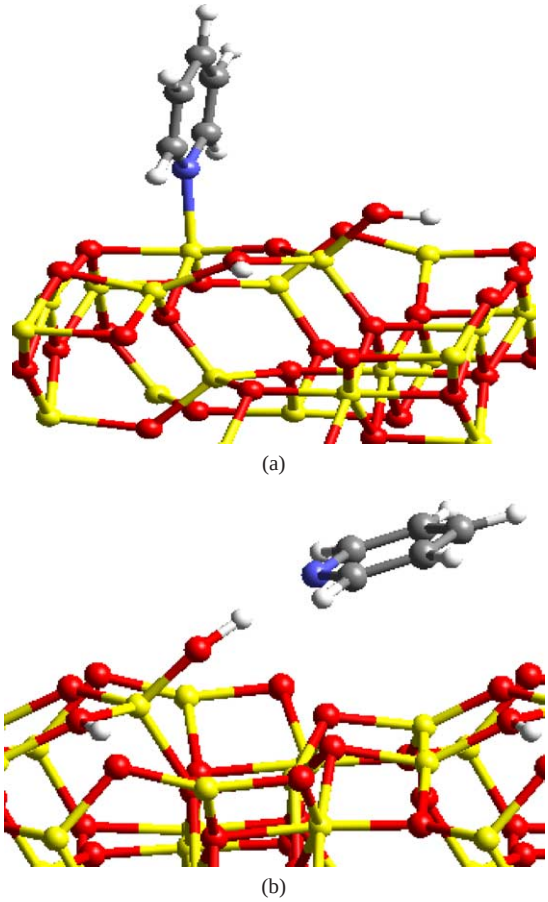

(a)

(b)

Fig. 11. Adsorption configurations of pyridine (a) on the Al_{IV} site and (b) on the HO–μ_1–Al_{IV} of the (110) surface.

19*a*, and 19*b* bands are less sensitive to the adsorption site. The assignment of the experimental bands on the Lewis sites is straightforward. Referring to the review of Morterra and Magnacca [19], we confirm unambiguously that the band at 1598 cm^{-1} (calc. 1606 cm^{-1}) corresponds to Al_V site, the band at 1610–1620 cm^{-1} (calc. 1617 cm^{-1}) to the Al_{IV} site (Fig. 11a), and the band at 1625 cm^{-1} to the Al_{III} site. We did not calculate this latter configuration, since both electronic analysis and CO adsorption have shown that the Al_{III} site is the most acidic. Thus, it is expected that the shift should be larger in this case. As a consequence, the stronger the Lewis site, the larger the calculated frequency shift of the 8*a* mode.

According to our calculations, pyridine also adsorbs on hydroxyl groups via O–H···N hydrogen bond. In most cases explored so far on thermodynamically stable hydrated surfaces, we found that the pyridinium ion is generally unstable (Table 8). Only when we tested the unlikely situation of one isolated μ_2–OH group, is proton transfer possible. The proton transfer is thus energetically unfavored, when compared to the O–H···N bond. In two cases (HO–μ_1–Al_{VI} and HO–μ_3–Al_{VI}), the frequency shift of the 8*a* band is weak. The bands are at 1593 and 1591 cm^{-1}, respectively, in agreement with the experimental bands at 1590–1594 cm^{-1} [13,19]. The behavior of the HO–μ_1–Al_{IV} group (Fig. 11b) is more specific: the 8*a* band shifts to 1610 cm^{-1}, within the region corresponding to Lewis site adsorption. This Brønsted site thus exhibits adsorption energy and a spectral signature close to the Lewis site. A corollary result concerns the downshift of OH-stretching frequencies upon pyridine adsorption due to hydrogen bonding: for the two HO–μ_1 groups, the frequency decreases to 3201 and 3081 cm^{-1} compared to 3842 and 3777 cm^{-1} before adsorption. These shifts are only in

qualitative agreement with the OH-stretching values of 3150 and 2920 cm^{-1} [13] found by HREELS on alumina thin films. Indeed, the comparison with such experiments must be carried out carefully. Instead of the great variety of OH groups traditionally observed on γ-alumina samples (Tables 5 and 8), a single peak at 3711 cm^{-1} is observed on such thin films, leading to the two frequencies at 3150 and 2920 cm^{-1} under pyridine pressure. As a consequence, either before or after pyridine adsorption, the OH-stretching bands involved in our calculations are not the same as that observed in [13]. We suggest that the frequency of this type of hydroxyls involved on the thin film might be of the HO–μ_2 type. However, further investigations are required to determined the precise nature of the aluminum oxide films, which does not seem to be of a γ-alumina type.

Finally, no significant perturbation of the HO–μ_3 group (at 3580 cm^{-1} after pyridine adsorption) is observed: the adsorption energy is low (-10 kJ mol^{-1}) and the OH stretch is not affected by the pyridine molecule. Hence, a striking result is that pyridine adsorbs the most weakly on HO–μ_3 groups, which are expected to be the most acidic (according to the value of the OH stretching as reported in Table 5). In contrast, pyridine adsorbs more strongly on HO–μ_1 groups. This result is explained by sterical constraints on HO–μ_3 and HO–μ_2 groups, which are far less accessible to pyridine than HO–μ_1 groups. HO–μ_3 and HO–μ_2 groups are deeply buried on the hydroxylated surfaces (see Fig. 8a and 8c). The more basic HO–μ_1 groups, pointing away from the surface, may develop a screening effect, thus preventing HO–μ_3 groups from pyridine adsorption. As a consequence, this effect may also explain that a clear correlation between the Brønsted acidity and the pyridine adsorption strength has not been observed experimentally [51].

4. Conclusions

Using the DFT approach combined with a thermodynamic model, we have established detailed models of γ-alumina surface structures under working conditions. Effects of morphology, temperature, and surface hydration have been analyzed: we showed that these factors determine the nature and concentration of the stable surface species, fundamental for a clear understanding γ-alumina surface chemistry. The robustness of the surface models is tested against an extensive list of published experimental data. This comparison enables an accurate assignment of OH-stretching frequencies and a precise description of the surface Brønsted acidity. We hope that we have convinced the reader that the Knözinger–Ratnasamy model [10] must be revised, despite its wide acceptance by the catalysis community. This model was the best possible approach at the time, and significant achievements were made. However, thanks to modern DFT simulations, the present work provides accurate and optimized structures of the surface sites under realistic working conditions of temperature and water pressure. This allows a step forward to a more rational understanding of γ-alumina acid–basic properties. The bulk model used for the surface construction is not a defective spinel-like structure, showing that our model allows the occupation by Al atoms of other than spinel sites. This is also a key difference among γ-alumina models reported so far. Our structure results from the simulated dehydration process of boehmite into γ-alumina, which is the industrial way of producing γ-alumina. Numerous correlations with experimental data are in favor of such a model:

(i) bulk properties such as Al atom site distribution (given by NMR and XRD), bulk modulus, or electronic density,
(ii) morphology properties as inherited from the boehmite morphology, and
(iii) acid–basic surface properties characterized by OH-stretching vibrations and probe molecules adsorption.

With respect to the latter results, the simulations allow a rationalization of the interpretation of IR experiments based on probe molecule adsorption, such as CO and pyridine, and a better understanding of the surface chemical properties of γ-alumina as a function of pretreatment temperature.

Finally, we hope that this work opens up new ways of investigating support effects as they occur in real industrial catalysts. A systematic comparison with another important oxide catalytic support, anatase–TiO_2, has been undertaken recently [52,53]. Such approaches will provide new concepts necessary for a more rational understanding of support effects in catalysis.

Acknowledgments

This work was undertaken within the Groupement de Recherche Européen “Dynamique Moléculaire Quantique Appliquée à la Catalyse,” a joint project of IFP-CNRS-TOTAL-Universität Wien. The authors thank the Institut du Développement et des Ressources en Informatique Scientifique (IDRIS) at Orsay (Project 609) for providing computational resources.

References

[1] G. Ertl, H. Knözinger, J. Weitkamp, The Handbook of Heterogeneous Catalysis, Wiley–VCH, Weinheim, 1997.
[2] P. Euzen, P. Raybaud, X. Krokidis, H. Toulhoat, J.-L. Le Loarer, J.-P. Jolivet, C. Froidefond, in: F. Schüth, K. Sing, J. Weitkamp (Eds.), Handbook of Porous Materials, Wiley–VCH, Weinheim, 2002, p. 1591.
[3] B.C. Lippens, J.H. de Boer, Acta Crystallogr. 17 (1964) 1312.
[4] J. Hietala, A. Root, P. Knuuttila, J. Catal. 150 (1994) 46.
[5] E.C. DeCanio, J.C. Edwards, J.W. Bruno, J. Catal. 148 (1994) 76.
[6] D. Guillaume, S. Gautier, F. Alario, J.M. Devès, Oil Gas Sci. Technol.-Rev. IFP 54 (4) (1999) 537.
[7] W. Zhang, M. Sun, R. Prins, J. Phys. Chem. 106 (2002) 11,805.

[8] A.A. Tsyganenko, V.N. Filimonov, J. Mol. Struct. 19 (1973) 579.
[9] C. Morterra, G. Ghiotti, F. Boccuzzi, S. Coluccia, J. Catal. 51 (1978) 299.
[10] H. Knözinger, P. Ratnasamy, Catal. Rev.-Sci. Eng. 17 (1978) 31.
[11] G. Busca, V. Lorenzelli, V. Sanchez Escribano, R. Guidetti, J. Catal. 131 (1991) 167.
[12] A.B. Mohammed Saad, V.A. Ivano, J.C. Lavalley, P. Nortier, F. Luck, Appl. Catal. 94 (1993) 71.
[13] K.A. Laynman, M.M. Ivey, J.C. Hemminger, J. Phys. Chem. B 107 (2003) 8538.
[14] M.C. Abello, A.P. Velasco, O.F. Gorriz, J.B. Rivarola, Appl. Catal. A 129 (1995) 93.
[15] B.A. Hendriksen, D.R. Pearce, R. Rudham, J. Catal. 24 (1972) 82.
[16] A. Auroux, M. Muscas, D.J. Coster, J.J. Fripiat, Catal. Lett. 28 (1994) 179.
[17] J.M. McHale, A. Navrotsky, A.J. Perrotta, J. Phys. Chem. B 101 (1997) 603.
[18] B. Ealet, M.H. Elyakhlouffi, E. Gillet, M. Ricci, Thin Solid Films 250 (1994) 92.
[19] C. Morterra, G. Magnacca, Catal. Today 27 (1996) 497.
[20] M. Digne, P. Sautet, P. Raybaud, P. Euzen, H. Toulhoat, J. Catal. 211 (2002) 1.
[21] M.B. Fleisher, L.O. Golender, M.V. Shimanskaya, J. Chem. Soc., Faraday Trans. 87 (1991) 745.
[22] J. Fernández Sanz, H. Rabaâ, F.M. Poveda, A.M. Márquez, C.J. Calzado, Int. J. Quantum Chem. 70 (1998) 359.
[23] K. Sohlberg, S.J. Pennycook, S.T. Pantelides, J. Am. Chem. Soc. 121 (1999) 10,999.
[24] A. Ionescu, A. Allouche, J.-P. Aycard, M. Rajzmann, F. Hutschka, J. Phys. Chem. B 106 (2002) 9359.
[25] X. Krokidis, P. Raybaud, A.-E. Gobichon, B. Rebours, P. Euzen, H. Toulhoat, J. Phys. Chem. B 105 (2001) 5121.
[26] G. Kresse, J. Furthmüller, Comput. Mater. Sci. 6 (1996) 15.
[27] G. Kresse, J. Furthmüller, Phys. Rev. B 54 (1996) 11,961.
[28] J.P. Perdew, J.A. Chevary, S.H. Vosko, K.A. Jackson, M.R. Pedersen, D.J. Singh, C. Frolhais, Phys. Rev. B 46 (1992) 6671.
[29] G. Kresse, J. Hafner, Phys. Rev. B 47 (1993) 558; Phys. Rev. B 48 (1993) 13,115; Phys. Rev. B 49 (1994) 14,251.
[30] P. Raybaud, M. Digne, R. Iftimie, W. Wellens, P. Euzen, H. Toulhoat, J. Catal. 201 (2001) 236.
[31] Y. Jeanvoine, J.G. Ángyán, G. Kresse, J. Hafner, J. Phys. Chem. B 102 (1998) 5573.
[32] T. Demuth, J. Hafner, L. Benco, H. Toulhoat, J. Phys. Chem. B 104 (2000) 4593.
[33] R.S. Zhou, R.L. Snyder, Acta Crystallogr. B 47 (1991) 617.
[34] C. Wolverton, K.C. Hass, Phys. Rev. B 63 (2001) 24,102.
[35] G. Gutiérrez, A. Taga, B. Johansson, Phys. Rev. B 65 (2000) 012,101.
[36] S.J. Wilson, J. Solid State Chem. 30 (1979) 247.
[37] C. Pecharromán, I. Sobrados, J.E. Iglesias, T. Gonzáles-Carreño, J. Sanz, J. Phys. Chem. B 103 (1999) 6160.
[38] C.S. John, N.C.M. Alma, G.R. Hays, Appl. Catal. 6 (1983) 341.
[39] M.H. Lee, C.F. Cheng, V. Heine, J. Klinowski, Chem. Phys. Lett. 265 (1997) 673.
[40] M.R. Gallas, G.J. Piermarini, J. Am. Ceram. Soc. 77 (1994) 2917.
[41] S.-D. Mo, Y.-N. Xu, W.-Y. Ching, J. Am. Ceram. Soc. 80 (1997) 1193.
[42] J.P. Beaufils, Y. Barbaux, J. Chim. Phys. 78 (1981) 347.
[43] P. Nortier, P. Fourre, A.B. Mohammed Saad, O. Saur, J.-C. Lavalley, App. Catal. 61 (1990) 141.
[44] X.-G. Wang, A. Chaka, M. Scheffler, Phys. Rev. Lett. 84 (2000) 3650.
[45] C. Noguera, J. Phys.: Condens. Matter 12 (2000) R367.
[46] A. Zecchina, P. Escalona, C. Otero Areán, J. Catal. 107 (1987) 244.
[47] J.H. Ballinger, J.J. Yates, Langmuir 7 (1991) 3041.
[48] L. Machese, S. Bordiga, S. Coluccia, G. Marta, A. Zecchina, J. Chem. Soc., Faraday Trans. 89 (1993) 3483.
[49] C. Morterra, V. Bolis, G. Magnacca, Langmuir 10 (1994) 1812.
[50] R. Métivier, I. Leray, M. Roy-Auberger, N. Zanier-Szydlowski, B. Valeur, New J. Chem. 26 (2002) 411.
[51] X. Liu, R.E. Truitt, J. Am. Chem. Soc. 119 (1997) 9856.
[52] C. Arrouvel, M. Digne, M. Breysse, H. Toulhoat, P. Raybaud, J. Catal. 222 (2004) 152.
[53] C. Arrouvel, M. Breysse, H. Toulhoat, P. Raybaud, J. Catal. (2004), in press.